European Journal of Nuclear Medicine and Molecular Imaging (2021) 48:2363–2372
https://doi.org/10.1007/s00259-020-05124-y

ORIGINAL ARTICLE

Kinetic metrics of ^{18}F-FDG in normal human organs identified by systematic dynamic total-body positron emission tomography

Guobing Liu[1,2,3] · Hongrong Xu[4] · Pengcheng Hu[1,2,3] · Hui Tan[1,2,3] · Yiqiu Zhang[1,2,3] · Haojun Yu[1,2,3] · Xuening Li[4] · Hongcheng Shi[1,2,3]

Received: 15 June 2020 / Accepted: 15 November 2020 / Published online: 8 January 2021

Abstract

Purpose To investigate the kinetic metrics of 2-[^{18}F]-fluoro-2-deoxy-D-glucose (^{18}F-FDG) in normal organs by using dynamic total-body (TB) positron emission tomography (PET).

Methods Dynamic TB-PET was performed for nine healthy volunteers. Time-to-activity curves (TACs) were obtained by drawing regions of interest in the organs. A two-tissue compartment model was fitted for each tissue TAC. Constant rates, including k_1, k_2, and k_3, and the metabolic rate of FDG (MRFDG) were obtained. The parameter statistics, including the average, standard deviation, coefficient of variance, and inter-site and inter-individual variances, were compared.

Results Constant rates and MRFDG varied significantly among organs and subjects, but not among sides or sub-regions within an organ. The mean k_1 and k_2 ranged from 0.0158 min^{-1} in the right lower lung to 1.1883 min^{-1} in the anterior wall of the left ventricle (LV) myocardium and from 0.1116 min^{-1} in the left parietal white matter to 4.6272 min^{-1} in the left thyroid, respectively. The k_3 was lowest in the right upper area of the liver and highest in the septal wall of the LV myocardium. Mean MRFDG ranged from 23.1696 μmol/100 g/min in the parietal cortex to 0.5945 μmol/100 g/min in the lung. Four groups of organs with similar kinetic characteristics were identified: (1) the cerebral white matter, lung, liver, muscle, bone, and bone marrow; (2) cerebral and cerebellar cortex; (3) LV myocardium and thyroid; and (4) pancreas, spleen, and kidney.

Conclusion The kinetic rates and MRFDG significantly differed among organs. The kinetic metrics of FDG parameters in normal organs can serve as a reference for future dynamic PET imaging and research.

Keywords 2-[^{18}F]-Fluoro-2-deoxy-D-glucose (^{18}F-FDG) · Positron emission tomography (PET) · Dynamic imaging · Metabolic rate · Kinetic parameter

Introduction

A great advantage of positron emission tomography/computed tomography (PET/CT) over other imaging modalities is that it permits the measurement of physiological parameters, including pharmacokinetics and pharmacodynamics, through a dynamic study of tracer kinetics [1, 2]. Because of the limited axial field of view (AFOV) of conventional PET scanners (15 to 25 cm), dynamic imaging is limited to one bed position [3, 4]. Although whole-body dynamic imaging has been investigated using a multiple-bed multiple-pass imaging protocol, fast tracer dynamic capturing was not feasible due to limited temporal resolution and the sensitivity was reduced, resulting in a low signal-to-noise ratio for parametric imaging [3, 5].

In 2019, United Imaging Healthcare released the first total-body (TB) PET/CT scanner in the world with an AFOV of

Guobing Liu and Hongrong Xu contributed equally to this work.

This article is part of the Topical Collection on Radiopharmacy

✉ Xuening Li
li.xuening@zs-hospital.sh.cn

✉ Hongcheng Shi
shi.hongcheng@zs-hospital.sh.cn

1 Department of Nuclear Medicine, Zhongshan Hospital, Fudan University, No. 180 in Fenglin Road, Shanghai 200032, People's Republic of China

2 Institute of Nuclear Medicine, Fudan University, Shanghai 200032, China

3 Shanghai Institute of Medical Imaging, Shanghai 200032, China

4 Department of Clinical Pharmacology, Zhongshan Hospital, Fudan University, No. 180 in Fenglin Road, Shanghai 200032, People's Republic of China

194 cm, named uEXPLORER, which ushered the era of TB-PET [6]. This step allowing simultaneous TB coverage afforded an overall > 40-fold gain in effective sensitivity and a > 6-fold increase in the signal-to-noise ratio [7–9]. The improved sensitivity allows for more precise dynamic imaging of the entire body and kinetic analyses of the physiologies of all organs, simultaneously. An additional advantage was the ability to derive high-quality tracer input function from major arteries in PET images for pharmacokinetic studies, avoiding arterial cannulation for blood sampling [1, 8]. Furthermore, the introduction of TB-PET creates an innovative "multisystem biology" framework for studying the human body [8, 10].

2-[^{18}F]-Fluoro-2-deoxy-D-glucose (^{18}F-FDG) was called the century molecule, given its great contribution as a PET tracer for assessing various pathologies. Several studies have investigated the kinetic parameters of ^{18}F-FDG in the normal brain [11], myocardium [12, 13], liver [14–16], lung [16], and muscle [17]; however, these studies were limited by regional coverage and thus ignored the body as a whole. Besides, most input functions in these studies were derived from arterial blood sampling which was unsuitable for clinical practice. Thus, the present study had two major aims: to validate the efficiency of TB-PET for dynamic imaging and mathematical quantification of the kinetic parameters of ^{18}F-FDG without blood sampling, and to investigate the kinetic metrics of ^{18}F-FDG in normal human organs entirely and systematically.

Materials and methods

This descriptive study was approved by the institutional review board of Zhongshan Hospital, Fudan University (IRB number: B2019-160R). Written informed consent was obtained from all participants.

Participants

Nine healthy volunteers were enrolled, whose basic information is summarized in Table 1. The exclusion criteria were as follows: a history of malignancy or organ excision, acute inflammation, hyperthyroidism or hyperparathyroidism, abnormal serological liver enzyme levels, liver cirrhosis, diabetes, renal/heart failure, and body mass index (BMI, kg/m^2) > 25 or < 18. Twenty minutes before scanning, the volunteers were instructed to relax on a comfortable bed in a quiet room with low ambient light, wearing a patch over the eyes and plugs in the ears. During the study, participants were told to avoid movement and speaking but to stay awake.

Configuration of the TB-PET scanner

The TB-PET/CT scanner (uEXPLORER, United Imaging Healthcare) has a long AFOV and a transaxial FOV of 194 and 68.8 cm, respectively. For the PET detector, lutetium-yttrium oxyorthosilicate scintillator crystals with a size of 2.76 × 2.76 × 18.1 mm^3 are used, which are arrayed in detector blocks of 7 × 6 with a pitch of 2.85 mm. Each array is read out to a 4.6 × 6-mm^2 silicon photomultipliers. The PET scanner consists of eight axial ring units with an axial length, inter-unit gap, and inner-ring diameter of 24 cm, 2.5 mm, and 78.6 cm, respectively. Each ring has 24 detector modules and each module has 5 × 14 detector blocks. The time-of-flight (TOF) technique is used with a time and energy resolution of approximately 430 ps and 11.7%, respectively. The spatial resolution in the center of the FOV can reach up to 2.9 mm after the filtered-back-projection reconstruction. The maximal acceptance angle of the detector is approximately 57°. An 80-row, 160-slice CT scanner is integrated into this system.

Dynamic data acquisition and reconstruction

Before PET/CT scanning, weight, height, and blood glucose concentration were determined. The participants fasted for at least 6 h before the injection of ^{18}F-FDG at a dose of 1.85 MBq/kg. Considering the high sensitivity of the total-body PET scanner, which allowed for low-dose imaging, the injected dose was a half reduction of the full dose used for routine PET imaging at our department according to the guideline of the European Association of Nuclear Medicine for FDG-PET/CT oncological examinations [18]. Low-dose CT was performed for attenuation correction (AC). Then, 75-min dynamic PET scanning was started simultaneously with a bolus injection of ^{18}F-FDG by hand into a vein near the ankle. The images were corrected for radioactive decay, attenuation, scatter, and randoms, and were reconstructed into a 239 × 239 × 679 matrix with voxels of 2.85 mm^3 by the list-mode ordered subsets expectation maximization algorithm incorporating TOF and point spread function modeling (OSEMTOF-PSF) [1]. For dynamic analysis, the images were divided into 60 frames: every 5 s a frame for the initial 3 min (36 × 5 s) and every 3 min a frame thereafter until the end (24 × 180 s). Representative frames of PET images are shown in Fig. 1.

Generation of time-activity curves

The frame-divided images were transferred to a workstation (uWS-MI R001; United Imaging Healthcare, Shanghai, China) with the vendor-provided software for dynamic analysis. Regions of interest (ROIs) as large as possible were drawn within the organ boundary. We chose two-dimensional ROIs instead of three-dimensional ROIs to avoid including unwanted areas beyond the target organ. The ascending aorta was selected for generating the image-derived input function because of its superiority over the left ventricle, as shown in supplementary file 1. For the brain, ROIs were

Table 1 Basic information of the nine volunteers

Subject	Sex	Age (years)	Height (cm)	Weight (kg)	Blood glucose (mmol/L)	Injected dose (MBq)
1	Male	57	168.1	70.1	6.4	121.99
2	Male	61	163.1	64.6	4.9	113.63
3	Male	51	168	53.0	5.4	99.27
4	Male	67	171.5	71.8	6.5	127.61
5	Male	63	171.0	66.4	5.8	120.18
6	Male	70	163.0	58.5	6.1	107.34
7	Female	43	161.5	55.3	4.8	102.56
8	Male	51	163.7	55.1	6.1	102.19
9	Female	43	146.6	49.3	5.0	88.99
Average		53.5	164.1	60.2	5.6	107.56
SD		12.7	7.06	9.04	0.65	13.00

SD, standard deviation

drawn in the parietal cortex on both sides, adjacent white matter, and cerebellar cortex. We selected the parietal cortex to represent gray matter because FDG metabolism in this area is relatively less influenced by the visual and auditory senses. For the thyroid, ROIs were placed in the middle areas of each side; for the myocardium of the left ventricle (LV), the middle segments of the anterior, inferior, lateral, and septal walls were measured. For the lung, ROIs were placed in the external field of each lobe excluding large vessels, nodules, or inflammatory changes on CT; for the liver, ROIs were drawn in the upper, middle, and lower areas of the right lobe and middle area of the left-external lobe, avoiding any obvious abnormalities or vessels on CT. For the spleen, the ROI was placed in the area with the largest transaxial size; for the pancreas, the ROI was drawn in the body part. For the kidney, ROIs were drawn in the cortex of the middle levels on each side; for the bone, the ROI was placed in the 3rd lumbar body. For the skeletal muscle and bone marrow, average values from ROIs in bilateral psoas major muscles and bilateral medullary cavities in the upper areas of the femurs were measured, respectively. ROI delineation in each organ is illustrated in Fig. 2. The average radioactivity (kBq/mL) within each ROI at each frame was obtained for generating time-activity curves (TACs).

Mathematic model fitting and parameter generation

TAC data were uploaded to PMOD Kinetic Modeling (version 3.2, Zürich, Switzerland) for model fitting using the standard FDG two-tissue compartment model (Fig. 3). The temporal tissue activity of ^{18}F, C_{PET}, was related with the rate constants k_1, k_2, k_3, k_4, and νB, including whole-blood activity $C_{Blood}(t)$ for spillover correction and the plasma input curve

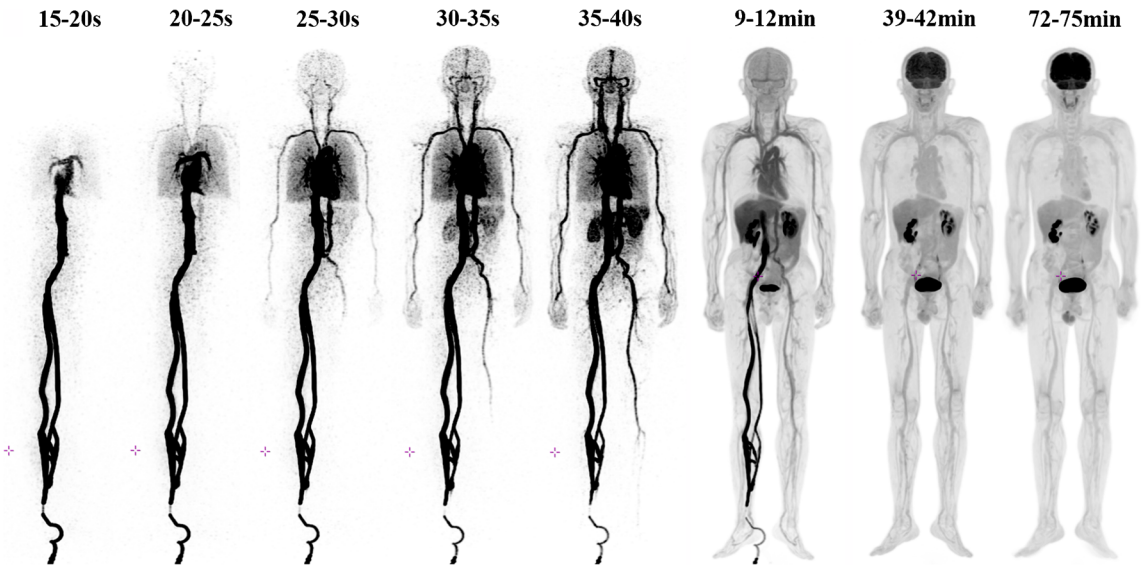

Fig. 1 Maximum intensity projection of selected dynamic reconstructed images

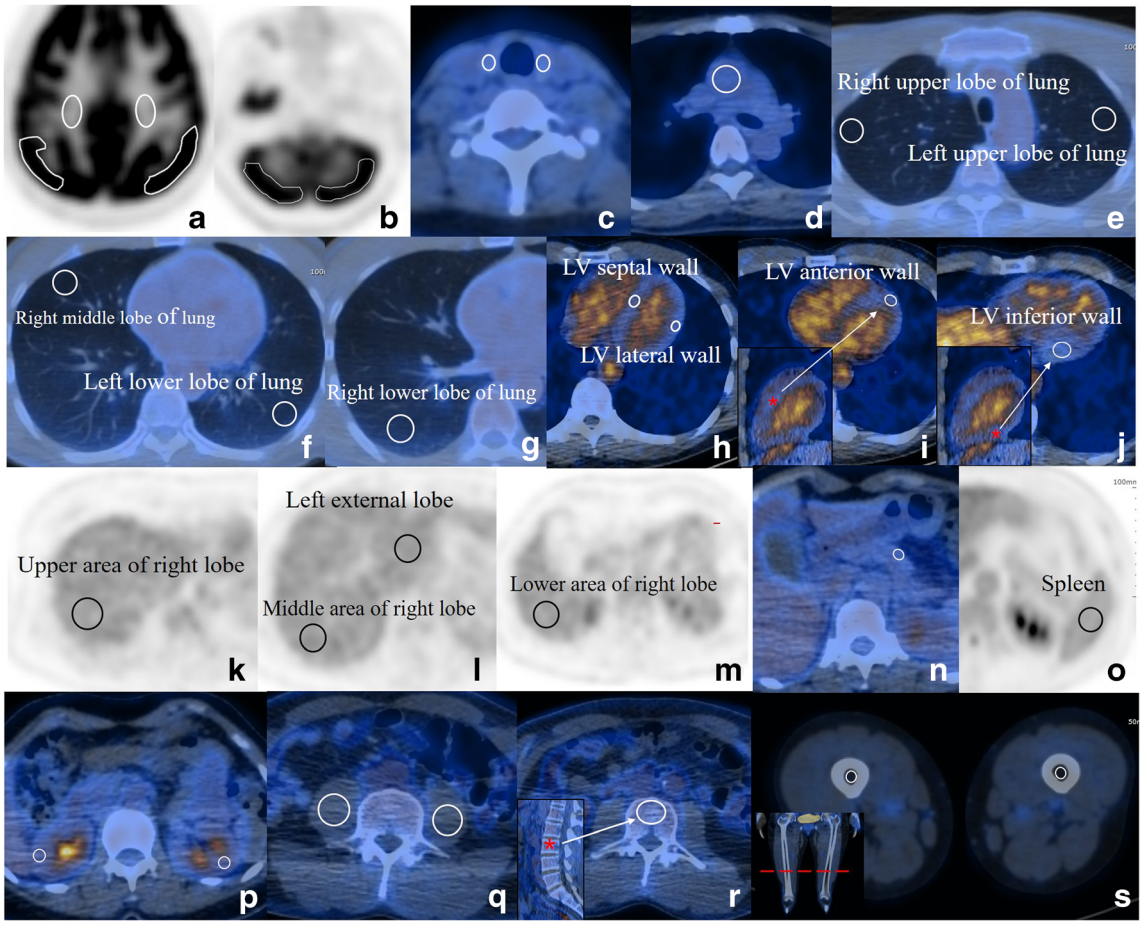

Fig. 2 Region of interest (ROI) delineation in the parietal cortex on both sides (irregular shapes in **a**), the white matter (ellipses in **a**), the cerebellar cortex (**b**), the thyroid (**c**), the ascending aorta (**d**), the lung (**e–g**), the left ventricle wall (**h–j**), the liver (**k–m**), the pancreas (**n**), the spleen (**o**), bilateral kidneys (**p**), bilateral psoas major muscles (**q**), the third lumbar body (**r**), and the bone marrow cavity of both femurs (**s**)

$C_P(t)$, as shown in the following equation:

$$C_{PET}(t) = \nu B \times C_{Blood}(t) + [k_1(1-\nu B) + \nu B(k_2+k_3+k_4)]\int_0^t C_P(\tau)d\tau + [\nu B(k_2 \times k_4) - k_1(k_3+k_4)(1-\nu B)]\int_0^t\int_0^\tau C_P(s)ds d\tau - (k_2+k_3+k_4)\int_0^t C_{PET}(\tau)d\tau - (k_2 \times k_4)\int_0^t\int_0^\tau C_{PET}(s)ds d\tau \quad (1)$$

The plasma input function, $C_P(t)$, was corrected from $C_{Blood}(t)$ according to Eq. 2 in the previous study [19], where the hematocrit was 0.42 for men and 0.36 for women, and the equilibration time constant was 0.2346 min^{-1} (Fig. 4). The νB indicates the fraction of blood volume in tissue. The constant rates indicate the transport of FDG forward (k_1) and backward (k_2) from plasma to tissue, FDG phosphorylation (k_3), and dephosphorylation (k_4). For each fitting, the TAC from the ascending aorta was selected for generating the input function. The regional metabolic rate of FDG (MRFDG) could be calculated using the following equation according to a previous study [20]:

$$\text{MRFDG} = \text{CGluP} \times \frac{k_1 \times k_3}{k_2 + k_3} \quad (2)$$

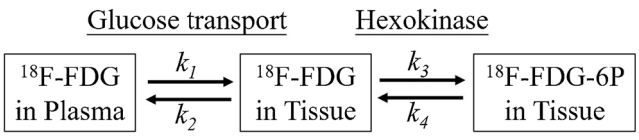

Fig. 3 Schematic diagram of the FDG two-tissue compartment kinetic model used in this study. The constant rates k_1 to k_4 indicate the transport of FDG forward and backward from plasma to tissue, FDG phosphorylation, and dephosphorylation, respectively

In addition, the index R^2 was selected for assessing the goodness-of-fit. Representative model fittings are shown in Fig. 5.

Statistical analysis

Summary statistics were presented as mean ± SD and coefficient of variation (CV) if necessary. Rate constants and MRFDG values of the organs were compared on the basis of differences among subjects and regions through factorial

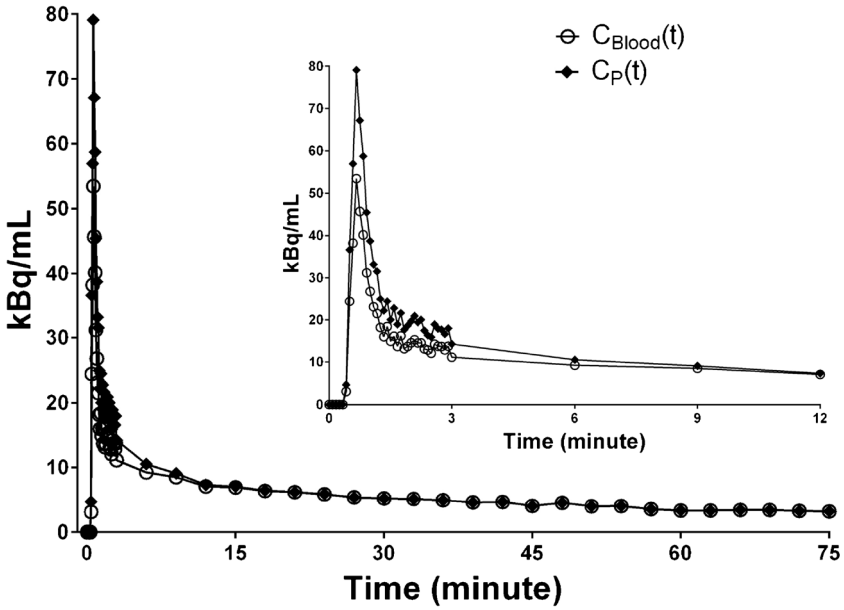

Fig. 4 Time course of radioactivity in whole blood ($C_{Blood}(t)$) and in corrected plasma ($C_P(t)$) in one of the participants in this study. The inserted image illustrates the curves for the first 12 min

analyses. Variances were compared using mixed models. Cluster analyses through iterative partitioning with the maximum likelihood criteria were performed to identify organs with similar kinetic characteristics. All statistical

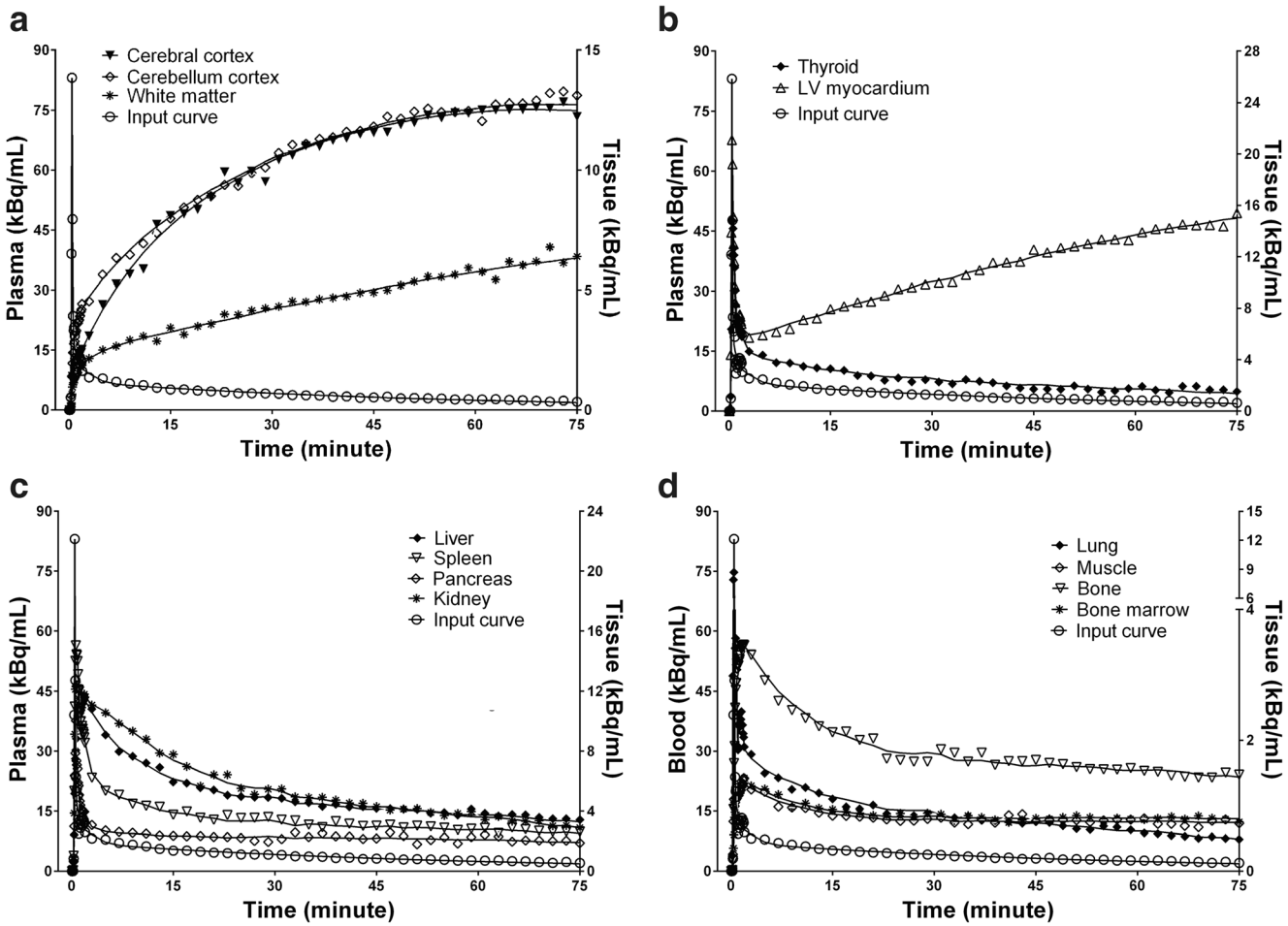

Fig. 5 Time courses and model fitting of ^{18}F-FDG concentrations in the organs of a 43-year-old female volunteer with a height of 161.5 cm and a weight of 55.3 kg. The injected dose of ^{18}F-FDG was 102.6 MBq. Individual symbols represent the original data

analyses were performed using SPSS 20 (IBM SPSS Inc., Chicago, IL, USA), and all hypothesis tests were two-sided with a significance level of 0.05.

Results

Summary statistics of the fitted constant rates are presented in Tables 2 and 3. Representative fitted curves are demonstrated in Fig. 3. All of the fitted models showed excellent goodness-of-fit ($R^2 > 0.93$; Table 2).

The constant rates varied to a great degree among organs, with mean k_1 ranging from 0.0158 min^{-1} in the right lower lobe of the lung to 1.1883 min^{-1} in the anterior wall of the LV myocardium, mean k_2 ranging from 0.1116 in the right parietal white matter to 4.6272 min^{-1} in the left lobe of the thyroid, and k_3 ranging from 0.0142 min^{-1} in the right upper area of the liver to 0.3413 min^{-1} in the septal wall of LV myocardium. No significant differences in constant rates among sites within an organ could be found. In contrast, the inter-individual variances of k constants were generally larger and contributed in remarkable proportions to the overall variances, with the inter-individual variances in k_3 of LV myocardium reaching statistical significance ($P < 0.001$). Of all the organs tested, the myocardium presented the largest inter-subject variance in terms of CV, which ranged from 67.4 to 91.6% for k_1, from 61.3 to 95.1% for k_2, and from 80.4 to 95.4% for k_3. These variances contributed to 31.6%, 71.4%, and 63.3% of the total variance of k_1, k_2, and k_3, respectively.

In most of the organs, the k_2 constants were much larger than the k_1 constants, potentially indicating a major role of ^{18}F-FDG clearance during the time course. The exceptional organ was the liver, in which k_2 (0.5089 ± 0.0793) was relatively close to k_1 (0.4134 ± 0.0473)), indicating that the FDG metabolism of the normal liver might remain stable for a long time.

Figure 6 shows the distribution of organs in three-dimensional rate-constant space and illustrates the maximum likelihood grouping. An optimum of four groups of organs was obtained, as shown in Table 4. The first group had the lowest k_1 and k_3 and consisted of the white matter of the brain, the lung, the liver, the muscle, the bone, and the bone marrow, representing a low level of metabolism; another group demonstrated k_1 values similar to those of organs from group 1, but with the lowest k_2 and the highest k_3, indicating high avidity of FDG, and it consisted of the cerebral and cerebellar cortices; a third group included the LV myocardium and the thyroid, which had the highest k_1 and k_2, but a relatively lower k_3, indicating rapid metabolism but low utilization of FDG; the last group, consisting of the pancreas, the spleen, and the kidney, was distinguished from the third group mainly by somewhat lower values from k_1 to k_3.

MRFDG values of the organs are summarized in Table 3. The discrepancies in MRFDG among organs were dramatic, ranging from the highest value of 23.1696 ± 3.3054 μmol/100 g/min in the parietal cortex to the lowest value of 0.5945 ± 0.4170 μmol/100 g/min in the lung. The other two organs that exhibited relatively high metabolic rates were the cerebellar cortex (22.2233 ± 2.7109 μmol/100 g/min) and the myocardium (17.9395 ± 13.4310 μmol/100 g/min). Although differences between both sides or among various sub-regions did not reach statistical significance in any organ, variations among individuals were quite marked, with variations in LV myocardium having reached statistical significance ($P < 0.001$). Similar to the constant rates described above, the LV myocardium exhibited the largest CVs (74.9% in average).

Discussion

In this study, we investigated the kinetic constant rates and FDG metabolic rates of normal organs in healthy volunteers simultaneously and systemically through the newly released simultaneous total-body PET/CT. The organs showed dramatically different kinetic characteristics, which may reflect the variable expression levels of glucose-6-phosphatase and glucose transporter in each organ. Meanwhile, some organs showed similar kinetic metrics. The exact rationale for these findings is hard to explain, but there may be a reflection of the inter-organ relationships in the kinetic metabolism of FDG in normal organs.

The results of this study are meaningful at least in three aspects. First, high-quality PET imaging relies on good contrast of FDG metabolism between target lesions and background normal tissue. The kinetic constant rates in normal organs can elucidate the dynamic changes in FDG uptake and provide information for determining the personalized starting time of PET acquisition. Second, knowledge of kinetic metrics of normal tissue as shown in the current study is helpful for parametric PET to be used as a method for "ultra-staging" [21], since kinetic changes of FDG in the tumor always occur early before it becomes a macroscopic lesion. Third, the kinetic method used in this study may be referred for pharmacokinetic studies of other positron radiotracers in the future.

Because arterial blood sampling is invasive to participants and may result in radiation exposure to the PET imaging staff, an alternative method using image-derived input functions (IDIFs) based on TACs from dynamic scan in areas of the ascending aorta, descending thoracic aorta, the heart, or the abdominal aorta has been investigated [21, 22]. Differences between arterial radioactivity measured in blood samples and that obtained from dynamic scans would not significantly influence the calculation of kinetic constant rates [23]. In

Table 2 Summary statistics of k_1 and k_2 constants in normal organs

Organs	Site	k_1 (min^{-1})						k_2 (min^{-1})						Mean R^2
		Mean ± SD	CV (%)	Inter-site var. (%)	*P*	Inter-subject var. (%)	*P*	Mean ± SD	CV (%)	Inter-site var. (%)	*P*	Inter-subject var. (%)	*P*	
Cortex	Av.	0.0896 ± 0.0225	25.2	0.07	0.887	72.9	0.092	0.2532 ± 0.1626	64.2	0.23	0.852	49.6	0.506	0.981
	L	0.0849 ± 0.0210	24.8					0.2311 ± 0.1819	78.7					0.969
	R	0.0864 ± 0.0344	39.8					0.2584 ± 0.1559	60.3					0.972
White matter	Av.	0.0337 ± 0.0080	23.8	5.6	0.360	46.5	0.515	0.1347 ± 0.0455	33.8	4.9	0.372	40.0	0.547	0.959
	L	0.0383 ± 0.0175	45.8					0.1427 ± 0.0663	46.5					0.949
	R	0.0323 ± 0.0054	16.7					0.1116 ± 0.0508	45.5					0.930
Cerebellum	Av.	0.1318 ± 0.0716	54.3	4.2	0.451	42.2	0.628	0.6280 ± 0.3728	59.4	2.1	0.590	44.7	0.594	0.977
	L	0.1215 ± 0.0352	29.0					0.5882 ± 0.4707	80.0					0.960
	R	0.2165 ± 0.1383	63.8					0.6421 ± 0.2786	43.4					0.963
Thyroid	Av.	0.9663 ± 0.3436	35.6	4.0	0.317	68.0	0.115	4.6042 ± 1.9598	42.6	8.6	0.470	66.2	0.056	0.945
	L	0.9437 ± 0.3043	32.2					4.6272 ± 1.8662	42.2					0.935
	R	0.7825 ± 0.5091	65.1					3.6008 ± 1.577	43.8					0.931
Myocardium	Av.	0.8162 ± 0.5912	72.4	11.9	0.196	31.6	0.155	3.4975 ± 2.240	64.0	6.3	0.170	71.4	0.060	0.973
	Septal	0.5021 ± 0.4590	91.4					2.3493 ± 2.2351	95.1					0.932
	Lateral	1.1576 ± 0.7713	66.6					4.4992 ± 2.7560	61.3					0.944
	Ant.	1.1883 ± 1.0881	91.6					3.9612 ± 2.5038	63.2					0.939
	Infer.	1.0998 ± 0.7411	67.4					4.4241 ± 2.7745	62.7					0.949
Lung	Av.	0.0143 ± 0.0083	58.2	9.4	0.425	15.2	0.601	0.3628 ± 0.2387	65.8	19.3	0.083	35.6	0.537	0.959
	LUL	0.0704 ± 0.0338	48.0					2.0805 ± 1.1433	54.9					0.935
	LLL	0.0345 ± 0.0208	60.3					0.7340 ± 0.3347	45.6					0.944
	RUL	0.0325 ± 0.0157	48.3					1.0993 ± 0.6124	55.7					0.939
	RML	0.0196 ± 0.0104	53.1					1.0760 ± 0.6898	64.1					0.941
	RLL	0.0158 ± 0.009	56.8					0.2942 ± 0.2130	72.4					0.944
Liver	Av.	0.4134 ± 0.0473	11.4	1.7	0.619	16.5	0.057	0.5089 ± 0.0793	15.6	1.4	0.384	22.3	0.071	0.935
	RU	0.4161 ± 0.0534	12.8					0.5142 ± 0.0704	13.7					0.934
	RM	0.4296 ± 0.0549	12.7					0.5305 ± 0.0907	17.1					0.939
	RL	0.4276 ± 0.0488	11.4					0.5436 ± 0.0745	13.7					0.948
	LL	0.4367 ± 0.0793	18.1					0.5799 ± 0.1393	24.2					0.963
Spleen		0.8846 ± 0.2058	23.3	-	-	-	-	2.0169 ± 0.4931	24.5	-	-	-	-	0.947
Pancreas		0.3561 ± 0.1496	42.0	-	-	-	-	1.7077 ± 0.4647	27.2	-	-	-	-	0.938
Kidney	Av.	0.7023 ± 0.1919	27.3	29.5%	0.326	62.8	0.080	1.3542 ± 0.5321	39.3	0.04	0.846	42.9	0.083	0.964
	L	0.6628 ± 0.2918	44.0					1.3673 ± 0.8014	58.6					0.942
	R	0.752 ± 0.2014	26.8					1.434 ± 0.5806	40.5					0.943
Muscle	Av.	0.0263 ± 0.0156	59.1	-	-	-	-	0.3165 ± 0.1538	48.6	-	-	-	-	0.931
Bone		0.1544 ± 0.0484	31.3	-	-	-	-	0.7132 ± 0.2577	36.1	-	-	-	-	0.960
Bone marrow		0.0405 ± 0.0134	33.1	-	-	-	-	0.2901 ± 0.0898	31.0	-	-	-	-	0.936

SD, standard deviation; *CV*, coefficient of variance; *var.*, variance; *Av.*, average; *L*, left; *R*, right; *LUL*, left upper lobe; *LLL*, left lower lobe; *RUL*, right upper lobe; *RML*, right middle lobe; *RLL*, right lower lobe; *RU*, right upper area, *RM*, right middle area; *RL*, right lower area; *LL*, left lobe

contrast, we chose the ascending aorta for obtaining the IDIF, because it had been identified as having the strongest correlation with the findings from arterial sampling [22]. Besides, the ascending aorta shows advantages for generating IDIFs because of the possibility of defining relatively larger ROIs, allowing for better statistical properties and less spillover from the adjacent myocardium.

When measuring TACs in the brain, we did not conduct region segmentation, because the kinetic rates of the normal brain have been fully studied in previous reports [11, 24]. The mean values of constant rates in the brain identified in the current study are in good agreement with those found by Heiss et al. [11] and Huang et al. [24] for the cerebral cortex ($k_1 = 0.0963\ min^{-1}$, $k_2 = 0.1359\ min^{-1}$, $k_3 = 0.0668\ min^{-1}$) and white matter ($k_1 = 0.0542\ min^{-1}$, $k_2 = 0.1181\ min^{-1}$, $k_3 = 0.0443\ min^{-1}$). The slight differences can be explained by the IDIF method and the more sensitive PET scanner used in the current study.

Several studies have investigated the constant rates of the normal liver and reported different results for k_1 ($0.4 \sim 0.9\ min^{-1}$), k_2 ($0.5 \sim 1.0\ min^{-1}$), and k_3 ($0.005 \sim 0.02\ min^{-1}$) [14, 15]. The kinetic rates identified in the current study ($k_1 = 0.4134\ min^{-1}$, $k_2 = 0.5089\ min^{-1}$, $k_3 = 0.0129\ min^{-1}$) were within these ranges and were in close agreement with the results ($k_1 = 0.41\ min^{-1}$, $k_2 = 0.5$, and $k_3 = 0.02\ min^{-1}$) obtained if a single IDIF from the artery was used when performing model fitting [14]. In addition, the relatively smaller values of k_1 and k_2 correspond more to the actual FDG metabolism in the normal liver, which is generally low and relatively stable over a long time (at least 3 h

Table 3 Summary statistics of k_3 constants and MRFDG in normal organs

Organs	Site	k_3 (min^{-1})						MRFDG (μmol/100 g/min)					
		Mean ± SD	CV (%)	Inter-site var. (%)	*P*	Inter-subject var. (%)	*P*	Mean ± SD	CV (%)	Inter-site var. (%)	*P*	Inter-subject var. (%)	*P*
Cortex	Av.	0.2213 ± 0.1190	53.8	1.3	0.852	76.4	0.071	23.1696 ± 3.3054	14.3	0.04	0.885	65.9	0.102
	L	0.2128 ± 0.1345	63.2					22.7188 ± 3.9295	17.3				
	R	0.1954 ± 0.1403	71.8					22.5922 ± 2.7542	12.2				
White matter	Av.	0.0482 ± 0.0151	31.3	8.4	0.362	39.8	0.622	7.6003 ± 1.5807	20.8	0.51	0.821	25.3	0.925
	L	0.0387 ± 0.0186	48.1					7.433 ± 1.9172	25.8				
	R	0.0621 ± 0.0271	43.6					7.6585 ± 1.3975	18.2				
Cerebellum	Av.	0.1870 ± 0.1103	59.0	2.3	0.418	77.7	0.078	22.2233 ± 2.7109	12.2	0.55	0.686	74.6	0.071
	L	0.1997 ± 0.1522	76.2					22.1618 ± 4.2967	19.4				
	R	0.1438 ± 0.0731	50.8					21.6801 ± 2.303	10.6				
Thyroid	Av.	0.0748 ± 0.0317	42.4	7.8	0.151	67.5	0.089	10.6186 ± 5.3299	50.2	0.54	0.778	48.4	0.529
	L	0.0722 ± 0.0255	35.3					9.4204 ± 4.3336	46.0				
	R	0.1073 ± 0.0870	81.1					9.9675 ± 3.4687	34.8				
Myocardium	Av.	0.1909 ± 0.1013	53.1	4.9	0.169	63.3	< 0.001	17.9395 ± 13.4310	74.9	2.4	0.187	86.4	< 0.001
	Septal	0.3413 ± 0.2744	80.4					19.6728 ± 16.8183	85.5				
	Lateral	0.1999 ± 0.1848	92.4					20.8959 ± 15.4944	74.2				
	Anterior	0.1743 ± 0.1451	83.2					15.3442 ± 14.0936	91.8				
	Inferior	0.1609 ± 0.1535	95.4					17.1909 ± 10.8638	63.2				
Lung	Av.	0.0307 ± 0.0240	78.2	6.6	0.611	15.4	0.614	0.5945 ± 0.4170	70.1	9.2	0.445	13.7	0.682
	LUL	0.0538 ± 0.0441	82.0					0.6962 ± 0.4731	68.0				
	LLL	0.0459 ± 0.0247	53.8					0.7216 ± 0.5562	77.1				
	RUL	0.0601 ± 0.0446	74.2					0.8717 ± 0.7495	86.0				
	RML	0.0853 ± 0.0702	82.3					0.3221 ± 0.1986	61.7				
	RLL	0.0671 ± 0.0207	30.8					1.0169 ± 0.8009	78.8				
Liver	Av.	0.0129 ± 0.0065	50.5	10.9	0.105	27.7	0.064	5.224 ± 2.6668	51.0	6.9	0.095	39.9	0.115
	RU	0.0142 ± 0.0047	32.8					5.684 ± 1.9006	33.4				
	RM	0.0149 ± 0.0054	36.3					5.9637 ± 2.0605	34.6				
	RL	0.0158 ± 0.0084	52.9					6.0714 ± 2.952	48.6				
	L	0.0221 ± 0.0155	70.0					7.4343 ± 3.3576	45.2				
Spleen		0.0415 ± 0.0245	59.0	-	-	-	-	9.4001 ± 4.5722	48.6	-	-	-	-
Pancreas		0.0787 ± 0.0336	42.7	-	-	-	-	8.2122 ± 4.0378	49.2	-	-	-	-
Kidney	Av.	0.1778 ± 0.1376	77.4	1.9	0.459	72.4	0.081	9.1456 ± 6.4375	70.4	0.39	0.674	50.1	0.089
	L	0.2384 ± 0.2050	86.0					13.3018 ± 9.2816	69.8				
	R	0.1777 ± 0.1258	70.8					8.2030 ± 6.1255	74.7				
Muscle		0.0461 ± 0.0263	57.0	-	-	-	-	1.8139 ± 0.7345	40.5	-	-	-	-
Bone		0.0458 ± 0.0151	32.9	-	-	-	-	4.997 ± 1.1549	23.1	-	-	-	-
Bone marrow		0.0189 ± 0.0054	28.7	-	-	-	-	1.3437 ± 0.4579	34.1	-	-	-	-

SD, standard deviation; *CV*, coefficient of variance; *var.*, variance; *Av.*, average; *L*, left; *R*, right; *LUL*, left upper lobe; *LLL*, left lower lobe; *RUL*, right upper lobe; *RML*, right middle lobe; *RLL*, right lower lobe; *RU*, right upper area, *RM*, right middle area; *RL*, right lower area; *LL*, left lobe

after FDG injection) [25]. That is partially why the liver is most commonly considered as a reference organ for interpreting the metabolism of lesions in other organs [26].

Given its complexity of energy use, the LV myocardium always presents variable uptake of FDG, depending on the status of fasting or glucose loading [12, 13]. The constant rates in the current study are significantly different from those reported by Morita et al. [12] performed with glucose loading (k_1 = 0.041 min^{-1}, k_2 = 0.071 min^{-1}, k_3 = 0.0719 min^{-1}) but in close agreement with those reported by Choi et al. [13] in fasting status (k_1 = 0.835 min^{-1}, k_2 = 2.783 min^{-1}, k_3 = 0.186 min^{-1}). Even within the population group of fasting status, significant differences in FDG uptake [4] and kinetic rates (k_1 = 0.340 min^{-1}, k_2 = 1.035 min^{-1}, k_3 = 0.047 min^{-1}) [13] had been identified. All of these factors may have contributed to the large inter-subject variance in kinetic metrics in the LV myocardium demonstrated in the current study.

Several limitations of this study should be mentioned. First, due to the small sample size, investigating the differences in kinetic metrics between male and females, among different age groups, and across different BMI groups was not possible in this study. Second, all constant rates were obtained from participants under fasting status, and thus could not be used for reference for people after glucose loading. Third, when fitting the TACs of the liver, the dual-blood supply feature was not considered. Although dual-input models have been identified to be better than single-input models in relation to the adequacy of model fits, it seems more valid to approximate the liver blood supply by a single arterial input function given

Table 4 Mean constant rates of organs with similar kinetic characteristics as determined by a cluster analysis

Organs	k_1	k_2	k_3
Cerebral cortex Cerebellar cortex	0.1107	0.3406	0.2041
Thyroid Myocardium	0.8912	4.0508	0.1329
Spleen Pancreas	0.6477	1.6929	0.0993
Kidney			
White matter Lung	0.0971	0.3709	0.0339
Liver			
Muscle			
Bone			
Bone marrow			

that liver lesions are commonly supplied by the hepatic artery [14]. Finally, the tracer injection was performed through a vein near the ankle in this study; thus, dispersal of the bolus was inevitable. Fortunately, none of the participants showed varicose veins of the lower extremities, which may have minimized the impact of this factor.

Conclusions

In conclusion, the kinetic constant rates and MRFDG values of normal organs in the total body were different, indicating different kinetic characteristics. The distribution and normal range of kinetic metrics of FDG in normal organs identified in this study provide a reference for future dynamic PET imaging and research.

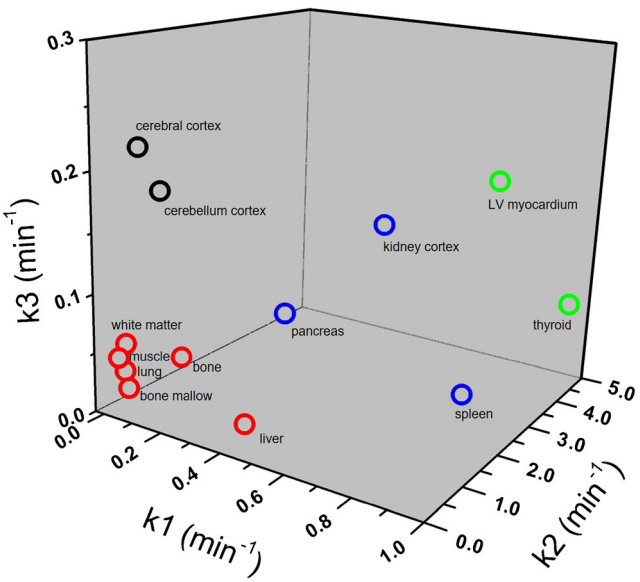

Fig. 6 Three-dimensional constant rate space illustrating four maximum likelihood clusters (in different colors) of organs. Only mean constant rates are shown in each of the organs

Supplementary Information The online version contains supplementary material available at https://doi.org/10.1007/s00259-020-05124-y.

Code availability Not applicable

Author contributions G.L. and H.S. had full access to all the data in the study and take responsibility for the integrity of the data and the accuracy of the data analysis. G.L., X.L., and H.S. were responsible for the concept and design of the study. G.L., P.H., Y.Z., and H.T. were involved in data acquisition. G.L., H.X., X.L., and H.S. were involved in data analysis and interpretation. G.L. and H.S. drafted the manuscript, and all authors revised it critically. G.L. and H.X. performed the statistical analysis. G.L. and H.S. obtained funding. X.L. and H.S. supervised the study.

Funding This study was funded by the Shanghai "Rising Stars of Medical Talent"—Youth Development Program (grant number: HWJRS2019-72), the Training Program for Excellent Young Medical Talents of Zhongshan Hospital of Fudan University (grant number: 2019ZSYQ28), the Shanghai Municipal Key Clinical Specialty Project (grant number: shslczdzk03401), the Major Science and Technology Projects for Major New Drug Creation (2019ZX09302001), the National Key Research and Development Program of China (grant number: 2016YFC0103908), the Three-year Action Plan of Clinical Skills and Innovation of Shanghai Hospital Development Center (grant number: SHDC2020CR3079B), and the Shanghai Science and Technology Committe (grant number: 20DZ2201800).

Data availability The datasets used and/or analyzed in the current study are available from the corresponding author on reasonable request.

Compliance with ethical standards

Conflict of interest The authors declare that they have no conflict of interest.

Ethics approval This study was approved by the Ethics Committee of Zhongshan Hospital of Fudan University (approval number: IRB2015-098). Written informed consent was obtained from all participants.

Consent to participate Written informed consent was obtained from the included patients for participation in this study.

Consent for publication The authors affirm that the human research participants provided informed consent for the publication of the studied data and the images in Fig. 1.

References

1. Zhang X, Xie Z, Berg E, Judenhofer MS, Liu W, Xu T, et al. Total-body dynamic reconstruction and parametric imaging on the uEXPLORER. J Nucl Med. 2020;61(2):285–91.
2. Cherry SR. In vivo molecular and genomic imaging: new challenges for imaging physics. Phys Med Biol. 2004;49(3):R13–48.
3. Rahmim A, Lodge MA, Karakatsanis NA, Panin VY, Zhou Y, McMillan A, et al. Dynamic whole-body PET imaging: principles,

potentials and applications. Eur J Nucl Med Mol Imaging. 2019;46(2):501–18.
4. Cheng G, Alavi A, Lim E, Werner TJ, Del Bello CV, Akers SR. Dynamic changes of FDG uptake and clearance in normal tissues. Mol Imaging Biol. 2013;15(3):345–52.
5. Fujimura Y, Kimura Y, Simeon FG, Dickstein LP, Pike VW, Innis RB, et al. Biodistribution and radiation dosimetry in humans of a new PET ligand, 18F-PBR06, to image translocator protein (18 kDa). J Nucl Med. 2010;51(1):145–9.
6. Badawi RD, Shi H, Hu P, Chen S, Xu T, Price PM, et al. First human imaging studies with the EXPLORER total-body PET scanner. J Nucl Med. 2019;60(3):299–303.
7. Zhang X, Badawi RD, Cherry SR, Qi J. Theoretical study of the benefit of long axial field-of-view PET on region of interest quantification. Phys Med Biol. 2018;63(13):767–70.
8. Cherry SR, Badawi RD, Karp JS, Moses WW, Price P, Jones T. Total-body imaging: transforming the role of positron emission tomography. Sci Transl Med. 2017;9(381):eaaf6169.
9. Surti S, Karp JS. Impact of detector design on imaging performance of a long axial field-of-view, whole-body PET scanner. Phys Med Biol. 2015;60(13):5343–58.
10. Cherry SR, Jones T, Karp JS, Qi J, Moses WW, Badawi RD. Total-Body PET: Maximizing sensitivity to create new opportunities for clinical research and patient care. J Nucl Med. 2018;59(1):3–12.
11. Heiss W, Pawlik G, Herholz K, Wagner R, Goldner H, Wienhard K. Regional kinetic constants and cerebral metabolic rate for glucose in normal human volunteers determined by dynamic positron emission tomography of [1Sp]-2-pluoro-2-deoxy-n-glucose. J Cereb Blood Flow Metab. 1984;4(2):212–23.
12. Morita K, Katoh C, Yoshinaga K, Noriyasu K, Mabuchi M, Tsukamoto T, et al. Quantitative analysis of myocardial glucose utilization in patients with left ventricular dysfunction by means of 18F-FDG dynamic positron tomography and three-compartment analysis. Eur J Nucl Med Mol Imaging. 2005;32(7):806–12.
13. Choi Y, Brunken RC, Hawkins RA, Huang SC, Buxton DB, Hoh CK, et al. Factors affecting myocardial 2-[F-18]fluoro-2-deoxy-D-glucose uptake in positron emission tomography studies of normal humans. Eur J Nucl Med. 1993;20(4):308–18.
14. Brix G, Ziegler SI, Bellemann ME, Doll J, Schosser R, Lucht R, et al. Quantification of [(18)F]FDG uptake in the normal liver using dynamic PET: impact and modeling of the dual hepatic blood supply. J Nucl Med. 2001;42(8):1265–73.
15. Choi Y, Hawkins RA, Huang SC, Brunken RC, Hoh CK, Messa C, et al. Evaluation of the effect of glucose ingestion and kinetic model configurations of FDG in the normal liver. J Nucl Med. 1994;35(5):818–23.
16. Hays MT, Segall GM. A mathematical model for the distribution of fluorodeoxyglucose in humans. J Nucl Med. 1999;40(8):1358–66.
17. Yokoyama I, Inoue Y, Moritan T, Ohtomo K, Nagai R. Measurement of skeletal muscle glucose utilization by dynamic 18F-FDG PET without arterial blood sampling. Nucl Med Commun. 2005;26(1):31–7.
18. Boellaard R, Delgado-Bolton R, Oyen WJ, Giammarile F, Tatsch K, Eschner W, et al. FDG PET/CT: EANM procedure guidelines for tumour imaging: version 2.0. Eur J Nucl Med Mol Imaging. 2015;42(2):328–54.
19. Wahl LM, Asselin MC, Nahmias C. Regions of interest in the venous sinuses as input functions for quantitative PET. J Nucl Med. 1999;40(10):1666–75.
20. Wu H, Dimitrakopoulou-Strauss A, Heichel TO, Lehner B, Bernd L, Ewerbeck V, et al. Quantitative evaluation of skeletal tumours with dynamic FDG PET: SUV in comparison to Patlak analysis. Eur J Nucl Med. 2001;28(6):704–10.
21. Price PM, Badawi RD, Cherry SR, Jones T. Ultra staging to unmask the prescribing of adjuvant therapy in cancer patients: the future opportunity to image micrometastases using total-body 18F-FDG PET scanning. J Nucl Med. 2014;55(4):696–7.
22. de Geus-Oei LF, Visser EP, Krabbe PF, van Hoorn BA, Koenders EB, Willemsen AT, et al. Comparison of image-derived and arterial input functions for estimating the rate of glucose metabolism in therapy-monitoring 18F-FDG PET studies. J Nucl Med. 2006;47(6):945–9.
23. Keiding S, Munk OL, Schiøtt KM, Hansen SB. Dynamic 2-[18F]fluoro-2-deoxy-d-glucose positron emission tomography of liver tumours without blood sampling. Eur J Nucl Med. 2000;27(4):407–12.
24. Huang SC, Phelps ME, Hoffman EJ, Sideris K, Selin CJ, Kuhl DE. Noninvasive determination of local cerebral metabolic rate of glucose in man. Am J Phys. 1980;238(1):E69–82.
25. Laffon E, Adhoute X, de Clermont H, Marthan R. Is liver SUV stable over time in (1)(8)F-FDG PET imaging? J Nucl Med Technol. 2011;39(4):258–63.
26. Wahl RL, Jacene H, Kasamon Y, Lodge MA. From RECIST to PERCIST: evolving considerations for PET response criteria in solid tumors. J Nucl Med. 2009;50(Suppl 1):122S–50S.